

Quantum Circuit Fidelity Improvement with Long Short-Term Memory Networks

Yikai Mao,^{1,*} Shaswot Shresthamali,¹ and Masaaki Kondo^{1,2}

¹Graduate School of Science and Technology, Keio University, Yokohama, Kanagawa 223-8522, Japan

²RIKEN Center for Computational Science, Kobe, Hyogo 650-0047, Japan

(Dated: March 31, 2023)

Quantum computing has entered the Noisy Intermediate-Scale Quantum (NISQ) era. Currently, the quantum processors we have are sensitive to environmental variables like radiation and temperature, thus producing noisy outputs. Although many proposed algorithms and applications exist for NISQ processors, we still face uncertainties when interpreting their noisy results. Specifically, how much confidence do we have in the quantum states we are picking as the output? This confidence is important since a NISQ computer will output a probability distribution of its qubit measurements, and it is sometimes hard to distinguish whether the distribution represents meaningful computation or just random noise. This paper presents a novel approach to attack this problem by framing quantum circuit fidelity prediction as a Time Series Forecasting problem, therefore making it possible to utilize the power of Long Short-Term Memory (LSTM) neural networks. A complete workflow to build the training circuit dataset and LSTM architecture is introduced, including an intuitive method of calculating the quantum circuit fidelity. The trained LSTM system, Q-fid, can predict the output fidelity of a quantum circuit running on a specific processor, without the need for any separate input of hardware calibration data or gate error rates. Evaluated on the QASMBench NISQ benchmark suite, Q-fid's prediction achieves an average RMSE of 0.0515, up to $24.7\times$ more accurate than the default Qiskit transpile tool `mapomatic`. When used to find the high-fidelity circuit layouts from the available circuit transpilation, Q-fid predicts the fidelity for the top 10% layouts with an average RMSE of 0.0252, up to $32.8\times$ more accurate than `mapomatic`.

I. INTRODUCTION

To outperform classical computers, quantum computers make use of the principles and phenomena of quantum mechanics. Traditionally, computers manipulate the classical bits in the binary basis, or 0/1 basis. When using a quantum computer, in addition to representing the classical 0/1 with its computational basis $|0\rangle/|1\rangle$, it also has the ability to perform calculations using an unlimited number of basis. For instance, the X-basis formed by the X gate in $|+\rangle/|-\rangle$. This flexible representation of data, combined with the ability to entangle multiple qubits, gives quantum computers the potential to achieve superpolynomial or even exponential speedups for traditionally hard computing problems, for example, Simon's problem [1].

Since Google fabricated the Sycamore processor back in 2018 and later announced Quantum Supremacy in 2019 [2], the field of quantum computing hardware has grown substantially. However, the current state of quantum processors is still far from perfect. The qubits can only hold their state information around the millisecond timescale due to external noises [3, 4], they have limited interconnectivity for multi-qubit quantum gates, and the error rate of the output is affected by various factors including circuit layout and physical qubit placement. To utilize these limited quantum computing resources, Noisy Intermediate-Scale Quantum (NISQ) [5] has offered a viable solution. NISQ computing uses error-mitigation

techniques to compensate for fragile qubits [6–8]. For example, performing repeated measurements to find high-probability outputs, or using multiple noisy physical qubits to represent one robust logical qubit [9, 10].

To implement a quantum circuit on a real NISQ processor, the circuit must be mapped onto the available physical qubits in accordance with their fixed connectivity configurations [11, 12], a process commonly known as transpilation. However, there are several challenges during this process. First, the qubits in one processor are not identical. Each of them has unique physical properties, typically categorized as $T1/T2$ (Thermal relaxation time) constants. These physical properties define the noise characteristics of the qubit, and they can change depending on the time of operation. *This causes the quantum circuits to exhibit different noise performances when they are placed on different qubits.* Second, due to the limited qubit connectivity, some quantum circuits need to be modified from the original design before implementing on real hardware. For example, adding SWAP gates to bring two qubits together which were otherwise physically apart. *Therefore, the accuracy of a quantum circuit can get compromised even if it is placed on high-quality qubits, due to the additional gate noise introduced by circuit transpilation.* Therefore, **to make the best use of current NISQ processors, we need a novel method that can accurately pick a high-fidelity circuit-to-qubit mapping from all the transpiled options.** This way we can efficiently retrieve high-quality measurements, without wasting quantum computing resources on testing noisy, error-prone transpilation.

The study of quantum circuit performance on real devices is still a very active area of research, and quantum

* ykmao@acsl.ics.keio.ac.jp

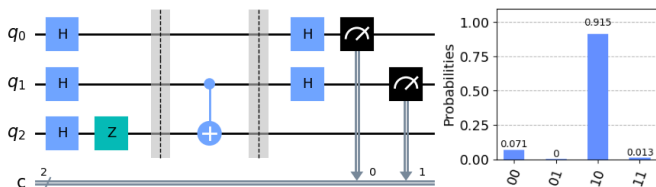


FIG. 1. Sample Circuit implementing the Bernstein-Vazirani Algorithm, the expected output should be $q_1 q_0 = |10\rangle$. q_2 is not measured so no result will be returned. Output distribution after running the circuit on real hardware (*ibm_nairobi*) is plotted on the right, notice the wrong measurements due to noise.

hardware providers are already offering tools to optimize circuits using simple noise models. The `mapomatic` tool is arguably the most commonly used quantum circuit optimization tool right now, as it is integrated inside the standard Qiskit transpiler [13], and is enabled by default for all the optimization levels during transpilation. However, it has some significant limitations. First, `mapomatic` accumulates the error rates of all the gates that appear in a quantum circuit to estimate its fidelity. These error data are obtained from the Randomized Benchmarking (RB) [14] protocol, which must be performed frequently to keep the data up to date. Second, the noise characteristic of a full quantum circuit is not simply the product of the individual gates [15], as there are still many error structures that are unmodeled. For example, unexpected resonance between qubit connections. Due to these errors, `mapomatic` cannot estimate the fidelity accurately and it only gives the relative performance comparison for a set of circuits with different physical mapping.

In this paper, we present an LSTM-based system: Q-fid, to accurately predict the fidelity of a quantum circuit. It eliminates the need for frequent calibration and Randomized Benchmarking experiments by actively learning qubit/gate operations from circuit execution data, without any separate input of system calibration parameters or error rates. Since the only input to Q-fid is the quantum circuit, it can be used on any gate-based quantum computer regardless of their implementation technology. Furthermore, because LSTM is lightweight and efficient, it can be integrated into the transpiling process with minimal added computation cost. Traditionally, a NISQ circuit requires hundreds to thousands of shots on a real processor to statistically estimate its correct output. With Q-fid’s prediction, we can save quantum computing resources by reducing the number of shots for a high-fidelity circuit, and rejecting execution when a circuit is predicted to have low-fidelity.

To evaluate its performance, we trained Q-fid on two of the IBM quantum processors: *ibm_nairobi* and *ibmq_montreal*. We used the `QASMBench` benchmark suite [16] with 25 NISQ algorithms from simple to complex to test Q-fid’s accuracy and compared it with `mapomatic`. Running individual circuits with fixed layouts and no transpiler optimizations on *ibm_nairobi*, Q-fid is able to

predict the circuit’s fidelity with an average RMSE of 0.0515, which is $5.70x$ more accurate than `mapomatic`. Among the 25 tested algorithms, Q-fid achieves $\geq 5.00x$ more accuracy than `mapomatic` in 11 of them, with the best prediction being $24.7x$ more accurate. On *ibmq_montreal*, when transpiler optimization is on, Q-fid correctly finds the top 10% of high-fidelity circuit layouts for all 25 algorithms. Within those top 10% of layouts, Q-fid’s predicted fidelity has an average RMSE of 0.0252, up to $32.8x$ more accurate than `mapomatic`.

The contributions of this work are listed below:

- We propose a simple and intuitive method to model a quantum circuit as a **text-based time series**. This method enables feeding the quantum circuits directly into an LSTM neural network, and it can be applied to **any gate-based quantum processor**, regardless of their implementation technology.
- We present the **discrete coefficient of determination** ($d-R^2$) as a new metric to quantify the fidelity of a noisy quantum circuit. $d-R^2$ clearly defines the uniform distribution as the **worst-case** output distribution for a quantum circuit, offering an intuitive baseline comparison for NISQ algorithm fidelities.
- We show that LSTM is effective in learning the properties of a qubit and a quantum gate from the quantum circuit itself. The trained system, **Q-fid**, can predict the performance of a quantum circuit without any separate input of hardware calibration data or gate error rates.
- We provide a **framework** to use LSTM for on-the-fly quantum circuit fidelity estimation. Including the **architecture** of the neural network, how to build the **dataset**, and the training **workflow**. We show that Randomized Benchmarking can be used to generate a comprehensive dataset for Q-fid.
- Experiments on **real NISQ algorithms** show that because Q-fid can accurately predict the fidelity of quantum circuits, we can retrieve more **high-fidelity, usable transpilation**s than `mapomatic` from a large set of transpiled circuits, thus increasing processor utilization by allowing more circuit placement options.

II. BACKGROUND

A. Quantum Circuits

For a universal gate-model Quantum Processing Unit (QPU), a Quantum Circuit (QC) describes a sequence of quantum gates applied to some specific quantum bits, or qubits. A qubit is the fundamental computing unit inside the QPU, in addition to representing classical binary states like $|0\rangle$ and $|1\rangle$, it can also stay in a quantum state

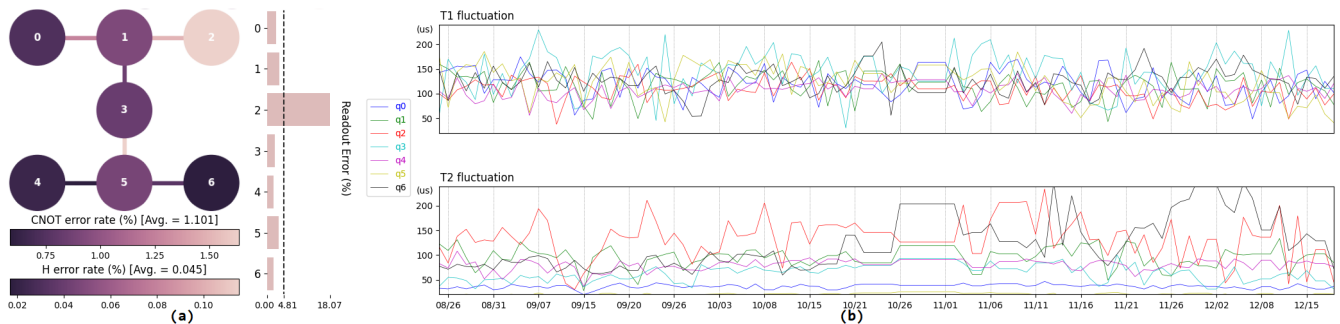


FIG. 2. (a) Error map of *ibm_nairobi* on Dec. 9, 2022, generated by the IBM Q platform [17]. (b) T_1/T_2 fluctuation of the 7 physical qubits inside *ibm_nairobi*. 100 data points were collected from Aug. 25 to Dec. 18, 2022. Note that data is not continuous due to scheduled/unscheduled system maintenance, for example around Nov. 1.

that is anywhere between $|0\rangle$ and $|1\rangle$. Similar to logic gates in a traditional computer that performs logic calculations, quantum gates perform quantum operations, which can be expressed as a matrix called a unitary operator. Since all unitary operators must be reversible, all quantum gates are also reversible. This means that it is always possible to apply the quantum gates in a QC in reverse order to return the qubits to their original state.

Typically, a QC involves three stages: state preparation, computation, and measurements. During state preparation, the input qubits are initialized into a specific state, for example, use a Hadamard gate to get superposition. The prepared qubits now sit on a special quantum basis, ready to enter the computation stage where they perform quantum transformations according to the implemented algorithm. Finally, the qubits of interest are measured, bringing them back from the quantum basis to the computational basis to reveal the classical information so that they can be interpreted either by a human or a classical computer, and continue to perform further tasks.

Figure 1 shows a sample implementation of the Bernstein-Vazirani Algorithm [18], divided nicely into the three stages mentioned previously. The three qubits $q_2q_1q_0$ are initialized to $| - + + \rangle$ from $|000\rangle$ in the first stage, after computation of a single Controlled-NOT (CNOT) gate, the qubits are returned to their original basis using Hadamard gates and then measured into the classical registers c_1c_0 to store the output.

B. NISQ Processors

All of the QPUs we have right now are NISQ processors, which have a limited number of qubits and are sensitive to external noise. Figure 2(a) gives the connection map of the 7 qubit QPU *ibm_nairobi* along with three major forms of possible error: readout, single-qubit error, and CNOT error. As shown in the connection map, qubit 2 has the worst readout error rate and H gate error rate. The CNOT connections between qubits 3 and 5 and qubits 1 to 2 are also significantly noisier than others.

It should be noted that the error rates are experimentally estimated using a protocol called Randomized Benchmarking (details in section III C), so the numbers will vary over time. Other mathematical models exist to characterize qubit qualities, and most of them involve measuring their T_1/T_2 constants. T_1 is commonly called the coherence time, it describes how long a qubit will relax from an excited state (e.g. $|1\rangle$) to the ground state (e.g. $|0\rangle$). T_2 is the decay time, which describes how long a qubit will lose its phase information. For example, decaying from $|+\rangle$ to $|0\rangle$. As shown in Figure 2(b), the T_1/T_2 constants can also fluctuate significantly, and it is hard to predict which physical qubit is more stable than others at a given time.

C. Circuit Transpilation

Due to the limited connectivity of current NISQ processors, it is not always possible to map a complex QC onto the processor directly. Take the connection map from Figure 2(a), notice the physical CNOT links only exist between neighboring qubits. So if a QC requires a CNOT gate between qubit 0 and qubit 3, additional operations must be added to the QC to compensate for the missed connection. This process of translating a hardware-agnostic QC description to fit the specified quantum device is referred to as transpilation.

To perform a long-distance CNOT gate in a superconducting quantum computer like *ibm_nairobi*, the transpiler can insert SWAP gates to virtually switch the position of the nonadjacent physical qubits, so they can use the existing CNOT links. However, in addition to connectivity restrictions, real quantum devices also have limited single-qubit gate availability. For example, at the time of writing, *ibm_nairobi* only supports four single qubit gates: ID, RZ, SX, X. To perform a high-level single-qubit operation like the Hadamard gate, the transpiler will need to decompose the operation using only the available gates. In *ibm_nairobi*, the Hadamard gate is realized by two $RZ(\pi/2)$ gates and one SX gate.

Typically, some level of QC optimization is also per-

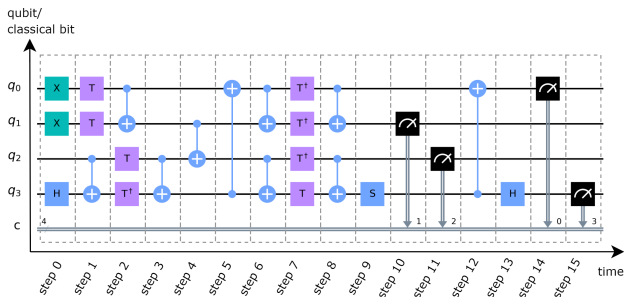


FIG. 3. Quantum circuit placed in a coordinate system with the y-axis as qubit/classical bit, and the x-axis as time. It can be viewed as the qubits being manipulated through each timestep from the left to the right on the time axis.

formed by the transpiler. One common optimization technique is CNOT reduction: because the SWAP gate is realized by three consecutive CNOT gates, it usually creates redundant gates that cancel each other due to the reversible nature of quantum operations, so they can be removed from the QC without affecting the final output states. There exist many other hardware-specific optimization techniques, they are provided by the transpiler developers for the users to choose based on different applications.

D. Long Short-term Memory Network

Neural Networks (NN) have demonstrated state-of-the-art performance in various tasks including Computer Vision (CV) and Natural Language Processing (NLP). Among numerous NN architectures, Long Short-term Memory (LSTM) network has been a popular choice for tasks related to time series processing, for example, weather forecasting and sentiment prediction. As a special type of Recurrent Neural Network (RNN), LSTM is designed to have “memory” of previous inputs, so that the final prediction is generated based on the full data sequence. Traditional RNNs cannot efficiently remember a long time series due to the vanishing gradient problem. However, this problem is solved in LSTM with the help of its specialized flow control mechanism. LSTM is composed of multiple building blocks called cells, inside each LSTM cell, three virtual gates are used to control the flow of data: the forget gate first determines if the data should be processed or ignored, then the input gate prepares the data for the cell to calculate the current cell state, this state is passed to the output gate along with the previous cell state to generate the value of the next state.

The connection between LSTM and QC analysis rises from the fact that a QC itself can be easily modeled as a time series. As figure 3 shows, the x-axis can be used to indicate the timesteps of a QC from start to end, with each timestep modeled as a “QC layer” containing all the gates in the y-axis. The layers are independent of each

other and have fixed widths, so the QC can be described as a two-dimensional time series with its width equal to the number of qubits in the circuit, and its length equal to the number of layers (sometimes referred to as the depth) of the circuit. Because LSTM is efficient in extracting features from a time series, it naturally becomes the preferred NN architecture for QC analysis.

III. DESIGN OF Q-FID

A. Concept

Q-fid is an LSTM network that takes a QC as input and predicts the output fidelity of this QC running on real hardware. Inspired by one of the most popular LSTM applications, Sentiment Analysis, the workflow of q-fid is very similar to the workflow of many common NLP tasks. In these tasks, the LSTM takes in a human sentence and gives a prediction based on different goals. For example, predict the meaning of the sentence in another language, return the answer to the sentence if it is a question, or whether the expressed sentiment is positive or negative. Although every individual word has its own definition, once combined together, they become elements of a single sentence where the meaning of the sentence must be inferred from the relationship between all of the words.

This concept fits surprisingly well if applied to a QC: Although every individual quantum gate has its own operation, once combined together, they become elements of a single circuit where the computation of the qubits must be interpreted after all quantum gates have been executed. Similar to a sentence where different orders of the same words can express different sentiments, the same set of quantum gates can perform different computations depending on their order in a circuit. Q-fid uses LSTM to catch this sequential feature of a QC, especially how the ordering of the quantum gates affects its final fidelity.

The architecture of Q-fid is simple and lightweight. The input layers first perform general pre-processing of the input QCs, then they are passed into the LSTM layer to extract long-term and short-term dependencies between the gates inside the QC. Finally, the output from the LSTM layer is passed into a series of fully-connected layers to generate the final prediction output. An overview of Q-fid’s architecture is shown in figure 4 from (g) to (i).

For Q-fid, the fidelity of a QC is a comparison of the two outputs: the reference output produced by the intended quantum operations from this QC without error, and the actual output produced by running the QC on a specific NISQ hardware. The output of a QC is a probability distribution of all the possible binary combinations, collected from running the QC with multiple shots and taking measurements repeatedly. For a QC running on noisy hardware, the binary state with the highest output probability is typically picked as the result of the QC.

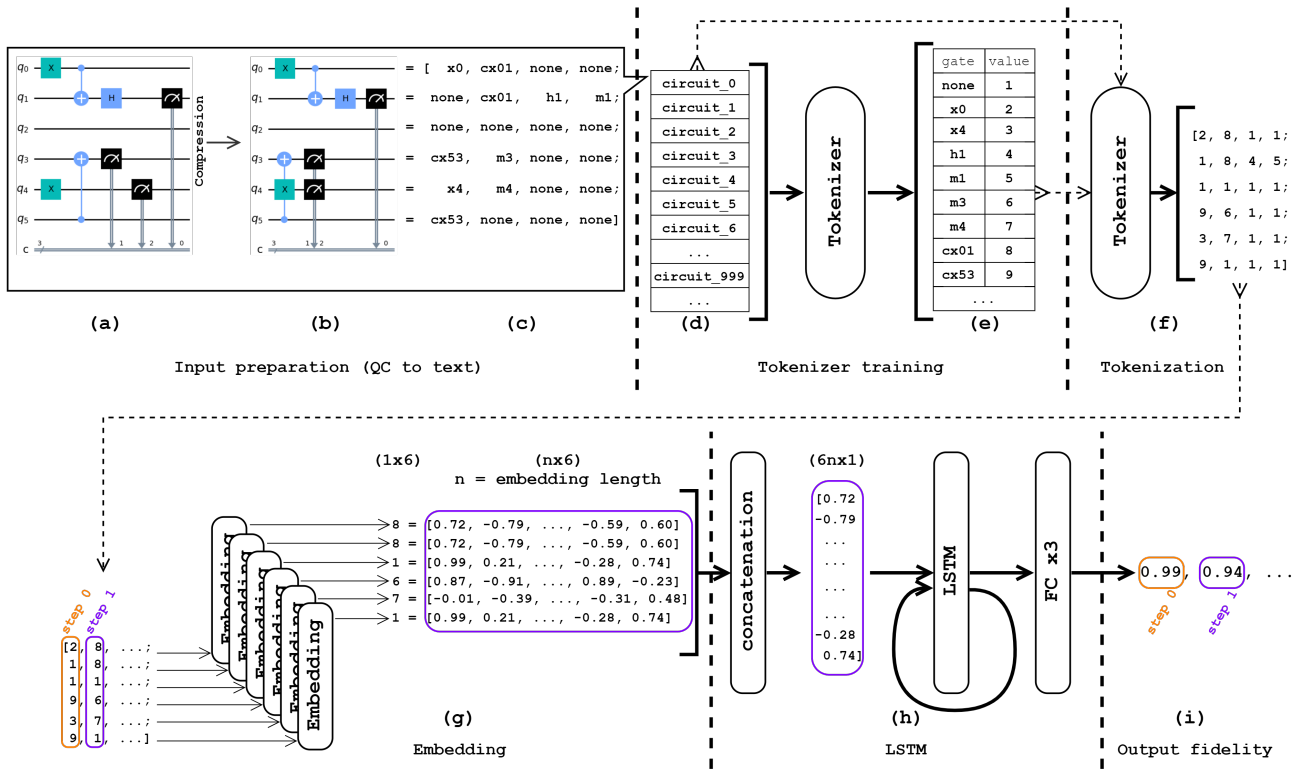


FIG. 4. Overview of Q-fid’s workflow. The first stage is input preparation (a, b, c), where the quantum circuits are compressed and mapped to their corresponding text label. The second stage is tokenizer training (d, e), the tokenizer will look through all the circuits in the dataset and assign each text label with an integer according to their appearing frequency. After the tokenizer is trained, it will use its internal dictionary to translate all of the circuits in the dataset to an integer representation, which is called tokenization (f). Q-fid’s neural network uses embedding (g) and LSTM (h) layers to encode the integer labels and then extract sequential and relationship information from the circuit, each prediction (i) is associated with one timestep in the circuit, when all the timesteps are processed by the LSTM, the output will be the final fidelity prediction for the full circuit.

In the case where a QC returns multiple high-probability binary states, the output of the QC can be understood as the “closest guess” to the correct answer. Nevertheless, the fidelity of a QC can be calculated by comparing the noisy output distribution to the noise-free output distribution, regardless of the number of output states. The detailed fidelity calculation proposed for Q-fid is explained in section III D.

A distinctive feature of Q-fid is that it does not require any prior knowledge of the processor’s calibration data ($T1/T2$, frequency, etc.) to make predictions. This design abstracts away the hardware details from the input, which greatly simplifies training and inference. To obtain the fidelity of a circuit as the ground truth training label for Q-fid, the circuit needs to be executed on the target processor to collect the output statistics. Since the only input to Q-fid is just the circuit itself, this execution can be performed either on the real processor or a noisy simulator, even if the noisy simulator does not explicitly provide the full device calibration data. Similarly, during inference, Q-fid can just use new circuit execution data to update its internal weights, therefore keeping itself up to date without the need to run extra calibration jobs.

B. Quantum Circuit as a Time Series

There exist many ways to describe a QC, either mathematical equations used by physicists or high-level programming languages used by computer scientists. But when used as the input to the LSTM, we need a text-based representation that describes a QC very close to a human sentence. Q-fid achieves this by using a simple and effective format to label the quantum gates inside a QC: a short string describing the quantum operation followed by the qubit index describing where the operation is executed on. For example, a Hadamard gate placed on qubit 2 is simply labeled as $h2$, a CNOT gate with control on qubit 0 and target on qubit 3 will be $cx03$. This format is very similar to many existing quantum programming languages including openQASM and Qiskit, so preparing an existing QC for q-fid is straightforward.

Q-fid has three steps to translate the QC to an LSTM-friendly format, a process commonly referred to as tokenization:

1. A tokenizer reviews the full QC dataset and builds a dictionary that maps each text label of a quantum gate to a unique integer. The labels are ranked ac-

ording to the frequency they appear in the circuit, with the most common appearing label mapped to 1. A special label in q-fid is `none`, which means the qubit is staying idle. This label is important because the qubit can decay and become noisier even when no gates are applied. An example of this workflow is shown in figure 4 from (a) to (f).

2. For a large QC dataset, the depth of the individual QCs can vary a lot. To improve the accuracy and efficiency of LSTM training, it is better to fix the number of time steps in the dataset. Once the maximum number of time steps is set, all of the integer-based QC vectors are either truncated or padded to the same depth. Specifically, the reason for the tokenizer to start from 1 is that 0 is reserved as the padding element, so that the LSTM knows it is not a label for a quantum gate and can safely skip it. Following the tradition of NLP [19], pre-padding and post-truncation are used.
3. After all the text labels are converted to integers, every QC in the dataset is now a dense vector. However, this is still not an efficient representation for input to q-fid. The integers do not possess any relationship or similarity information between different gates, so it is hard for the LSTM to learn the effect of interconnected quantum gates. This problem is solved by using word embeddings, a technique of using a higher dimension fixed-length vector to replace the integer encoding. The values of this embedding vector are trained at the same time with the LSTM, which helps q-fid capture more detailed information from the QC. The embedding layers are shown in figure 4(g).

One major advantage of this time series representation is that it can be applied to any QC regardless of their qubit technology. Whether the QC will be executed on trapped ion qubits or superconducting qubits, if the processor supports different basis gate groups, the tokenizer in step 1 can easily generate a new dictionary to map the gate labels to a new set of integers. This hardware-agnostic feature makes q-fid compatible with all gate-model quantum computers.

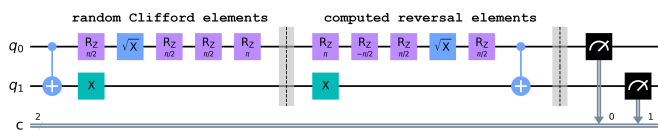


FIG. 5. Example of a Randomized Benchmarking circuit. The first part is the randomly generated Clifford gates, followed by the calculated reversal gates. The final measurement should be $|00\rangle$ if no errors occurred.

C. Randomized Benchmarking Circuits

Randomized Benchmarking (RB) [14, 20] is a protocol to estimate the error rates of the set of common quantum gates, usually called the Clifford gates. For IBM Q devices, this Clifford gate group includes $[X, Z, P, H, \text{CNOT}, \text{CZ}, \text{SWAP}]$ [21]. As mentioned in section II A, it is always possible to reverse a quantum circuit and return the qubits to their original states. Based on this principle, the RB protocol first generates a QC containing random quantum gates in the Clifford group, then it calculates a complementary gate sequence that can reverse the computation performed in the first QC. An example RB circuit is given in Figure 5. By applying the two generated QCs back-to-back, the full circuit is equivalent to an Identity operator so ideally any qubits involved in this circuit should never change their states when measured at the end. However, when executing an RB circuit on a NISQ processor, it is possible that the qubits cannot return to their initial state due to the noisy nature of the hardware. Therefore, by repeatedly running RB circuits and measuring the qubit outcomes, we can estimate the average sequence fidelity of the processor, and use that information in turn to predict the gate error rate, either for 2-qubit gates or single-qubit gates.

In q-fid, training an LSTM network to predict the fidelity of the full circuit requires a diversified dataset. Specifically, we evaluate diversity in two dimensions: depth and width. First, a deeper QC tends to have a lower fidelity in general, but the output from a deep circuit is not always unusable. Some deep but simple algorithms like the Quantum Phase Estimation (QPE) algorithm can be executed on noisy hardware and still give an output that is very likely to be the correct answer. To accurately predict the fidelity of circuits with various depths, the QC dataset should include samples that are also diverse in depth. Second, even for a shallow QC, using multiple qubits with complex connections will experience a higher error rate than a QC only using one qubit with no CNOT connection. To help the LSTM learn how multi-qubit operation affects fidelity, the QC dataset should contain both narrow and wide samples that utilize all the possible connections for a given QPU.

How to efficiently create a QC dataset that is large and diverse? It turns out that RB is an excellent tool to achieve this goal. The RB protocol can generate circuits based on many parameters including the number of qubits and RB circuit blocks, which provides the required diversity of width and depth for the dataset. Moreover, because the gates in RB circuits are randomly generated, we can guarantee that all available quantum gates for a specific QPU are covered, when the amount of generated circuits is sufficiently large (> 10000). Most of the computing complexity for generating RB circuits comes from calculating the final circuit block that reverses the previous operations, and it can be calculated efficiently in polynomial time, proved by the Gottesman-Knill theorem [22].

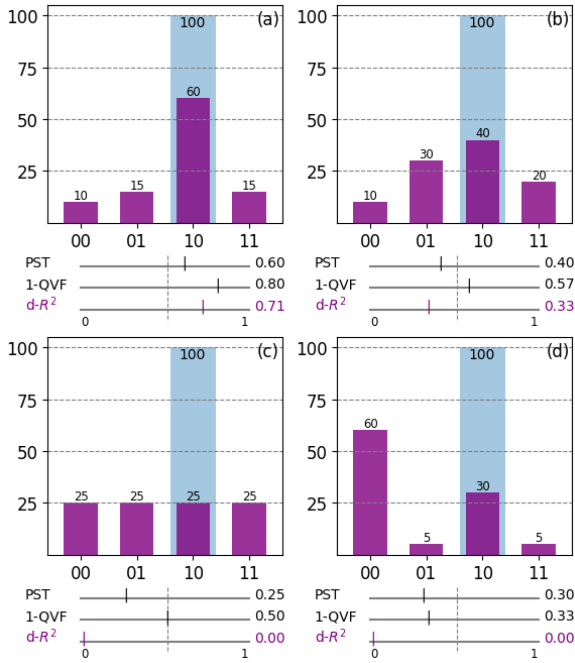


FIG. 6. Example measurement distributions after running the circuit in Fig. 1 with 100 shots. The expected measurement $|10\rangle$ is shown in light blue with 100 counts. The comparison of three QC fidelity metrics are shown below the bar graph, where 1 means the output is perfectly accurate.

Another important advantage of using RB to generate a QC dataset is that it greatly simplifies the fidelity score calculation. For a random QC, obtaining the fidelity score requires running the circuit twice: first, an ideal simulation assuming a noise-free environment, then a noisy execution, either on real hardware or through a noisy simulation. However, since all the QC samples in the q-fid dataset are RB circuits, if the qubits are initialized to $|0\dots 0\rangle$, we know for sure that the ideal output should also be $|0\dots 0\rangle$ based on the RB protocol. This means in order to generate the ground-truth labels for the RB samples, only one noisy execution is needed.

D. Discrete Coefficient of Determination ($d-R^2$)

In this work, we propose a slightly modified version of the *coefficient of determination* (R^2) as the standard metric for evaluating noisy QC fidelity. R^2 is commonly used in regression analysis to show the quality of how well a fitted line represents the original data, and it has been proven to be more robust and reliable than the other mean error-based metrics (MSE, MAE, etc.), especially on poor quality regressions [23]. Typically, $R^2 = 0$ indicates that the fitted line does not represent the original data at all, and $R^2 = 1$ indicates a perfect fit.

Most recent works [12, 24] use the Probability of Successful Trials (PST) as a metric to quantify the performance of a noisy QC, which is defined as the ratio of

the *number of successful trials* to the *total number of trials*. Although PST is easy to calculate and interpret, it does not represent the actual fidelity of a circuit. For example, figure 6(d) shows a distribution where the wrong state $|00\rangle$ is clearly overpowering the correct state $|10\rangle$. Since PST only focus on counting the correct states, it overestimates the fidelity of this result and gives a score very close to the tolerable result in figure 6(b). Other metrics have been proposed to replace PST, for example, the Quantum Vulnerability Factor (QVF) [25] and the Total Variation Distance (TVD) [26]. However, they do not offer a clear definition when multiple correct states are expected, which often happens for common NISQ algorithms like QAOA [27] and VQE [28].

Furthermore, when the QC outputs a uniform superposition like figure 6(c), QVF will yield a value of 0.5. It is impossible to pick a correct state from a uniform superposition output, and this output makes all the gates performed in the QC meaningless [29], as we can simply replace the QC with Hadamard gates applying to all qubits. Since outputs worse than a uniform superposition indicate wrong result (e.g. figure 6(d)) and should not be used to interpret the computation, we argue that the uniform superposition should be defined as the worst case output and have a 0 score in terms of fidelity.

Our modified version of R^2 is called discrete- R^2 , or $d-R^2$. compared with the other aforementioned metrics, $d-R^2$ has two important features that make it more suitable for NISQ fidelity analysis. First, it takes all the output states into consideration. In addition to checking how well the correct states are standing out, $d-R^2$ also penalizes wrong states when they should not appear in the measurements, which makes it work well with algorithms that output multiple correct states. Second, the baseline comparison model of the original R^2 metric ($R^2 = 0$) is a constant average line over the ground truth data. In $d-R^2$, this average line over the noise-free output distribution means exactly the uniform superposition, which conveniently matches our argument: a uniform superposition should be the worst-case output from a noisy QC.

To calculate $d-R^2$, we first have to calculate two Sum of Squares (SS):

$$\begin{aligned}
 \text{mean}(Y) &= \bar{Y} = \frac{1}{2^n} \sum_{i=0}^{2^n} Y_i \\
 SS_{\text{residual}} &= SSR = \sum_{i=0}^{2^n} (Y_i - y_i)^2 \\
 SS_{\text{total}} &= SST = \sum_{i=0}^{2^n} (Y_i - \bar{Y})^2
 \end{aligned} \tag{1}$$

Where n is the number of measured qubit(s), Y is the array containing all the measurement counts from the noise-free simulation, and y is the array containing all the measurement counts from the noisy output. Note that when calculating the subtractions, measurements

with 0 counts should also be included, and the two arrays must be aligned so that the measured qubit(s) match each other.

Then $d-R^2$ can be obtained as:

$$d-R^2 = \begin{cases} 1 - \frac{SSR}{SST}, & \text{if } SSR < SST \\ 0, & \text{otherwise} \end{cases} \quad (2)$$

- It is possible for $d-R^2$ to be negative without the bounding condition $SSR < SST$, this indicates that the distribution fits worse to the correct distribution than a uniform superposition, possibly caused by extremely noisy qubits or hardware faults. For example, figure 6(d) will give $d-R^2 = -0.14$ if the bounding condition is removed. Note if the goal when analyzing a QC is to find out which qubit is performing abnormally and causing the wrong output distribution like in figure 6(d), it is better to calculate PST values for individual qubits and check the one with the lowest score. PST works in this case because there are only two possible outcomes for a single qubit when measured: $|0\rangle$ and $|1\rangle$.
- A special case where $d-R^2$ is undefined happens when $SST = 0$ in equation 1. In the context of quantum computing, this indicates that the QC is **designed** to output a uniform superposition. This kind of circuit has some important applications, for example, it can be used as a Quantum Random Number Generator (QRNG) [30]. However, since it is very likely for an extremely noisy QC to also produce a random, uniformly distributed output, it is not possible to distinguish whether the circuit has been correctly executed, or simply output noise. In this case, $d-R^2$ becomes undefined by design because the QC should not be evaluated based on its fidelity, but rather on uniformity or randomness.

The interpretations for different $d-R^2$ values used in this paper are given in table I.

$d-R^2$	Interpretation
= 1	output is perfect, same as the noise-free simulation.
> 0.7 to ≤ 1	output is good, the circuit has high fidelity.
> 0.5 to ≤ 0.7	output quality is fair, contains noticeable noise.
> 0.3 to ≤ 0.5	output contains significant noise, interpret with caution.
> 0 to ≤ 0.3	output is extremely noisy, do not use.
= 0	output is no better than a uniform superposition.

TABLE I. discrete- R^2 values and interpretations

IV. EXPERIMENTAL METHODOLOGY

A. Dataset

We created two datasets based on two real IBM Quantum processors, *ibm_nairobi* and *ibmq_montreal*. The cir-

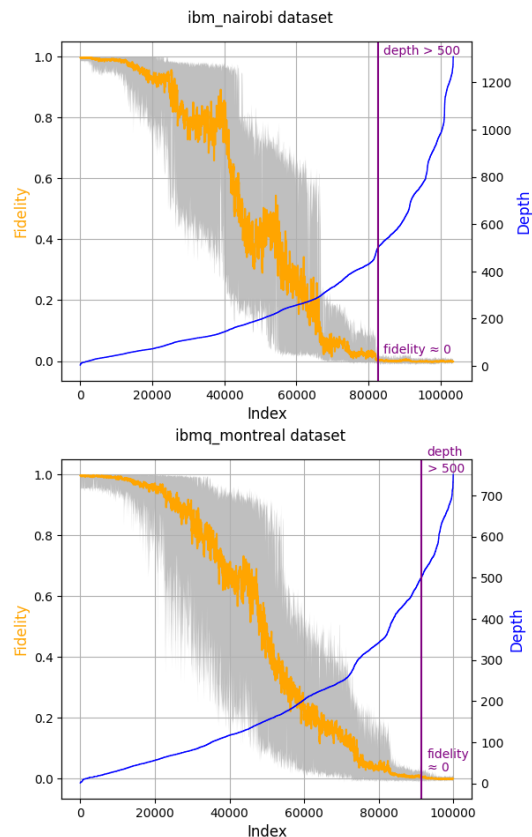


FIG. 7. Fidelity vs. depth for the two QC datasets. The depth is sorted from min to max, with a vertical purple line indicating the cut-off point of $depth = 500$. The fidelity has a very large variance so the raw data is shown in a gray envelope and an average line is shown in orange with a window size of 50.

cuits are randomly generated using the RB protocol, with the length of the RB sequence ranging from 1 to 5. We also change the number of active qubits when generating the RB circuits. For example, even though *ibm_nairobi* is a 7 qubit processor, we generated RB circuits that only require 1 qubit, 2 qubits, etc. The main reason for doing this is because placing the QC on different physical qubits in the same processor can yield different fidelity due to noise and manufacture variation. When the RB circuit only requires 1 active qubit, we can place the circuit on 7 different physical qubits on *ibm_nairobi*. This improves Q-fid's ability to learn the properties of individual qubits for a processor.

The *ibm_nairobi* QC dataset contains 103,500 circuits, and the *ibmq_montreal* QC dataset contains 100,000 circuits. All of the circuits are converted from Qiskit to a text-based representation described in section III B, then the fidelity scores are obtained using the Qiskit Aer simulator, with a noise model generated from the real hardware device. After analyzing the full circuit datasets, we removed all of the QCs that have a depth bigger than 500. This is because QCs that are very deep generally have a fidelity score extremely close to 0 (as shown in

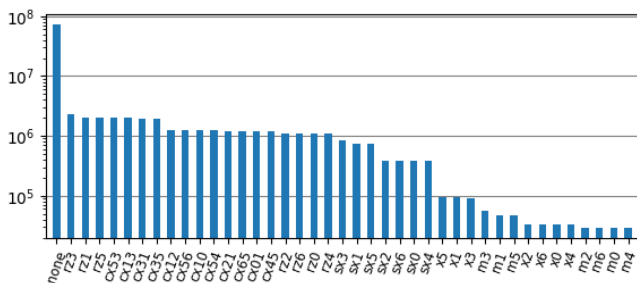


FIG. 8. The number of appearances for all the gate labels in the *ibm_nairobi* dataset. “m” stands for “measure”, so m0 means measure gate on qubit 0. The most common label is “none” with 72,124,510 appearances, and the least common label is “m4” with 29,528 appearances.

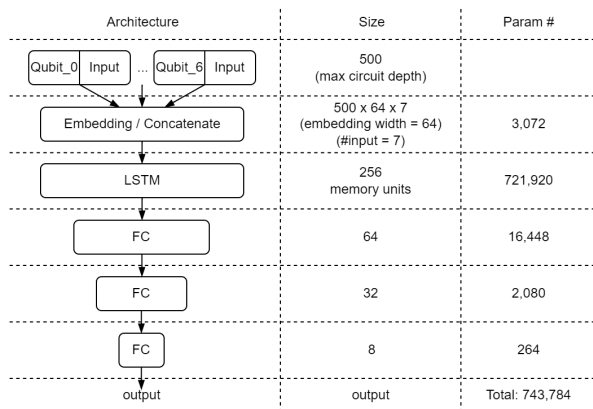


FIG. 9. Neural Network architecture of Q-fid. The number of input layers depends on the number of qubits inside a processor, this figure is showing the architecture for *ibm_nairobi*.

figure 7), it is not useful to force Q-fid to learn QCs that are known to have poor performance on current NISQ hardware. After trimming, the *ibm_nairobi* QC dataset has 82,644 circuits, and the *ibmq_montreal* QC dataset has 91,386 circuits.

Another advantage of representing QCs using text is that we can directly apply many existing NLP tools to analyze our dataset. By using the tokenizer mentioned in step 1 of section III B, we can see the statistics of the generated dictionary for the *ibm_nairobi* dataset in figure 8. First, all of the possible gates for *ibm_nairobi* are covered in the dataset, including the “none” label for no operation. Second, all seven qubits are also covered in the dataset, combined with the basis gates: rz, sx, x, measure, and bidirectional CNOT, giving a total of 41 entries for the tokenizer’s dictionary. This proves that RB is a suitable technique for generating QC training datasets, and it ensures Q-fid can learn the properties of every qubit/gate in the target quantum processor.

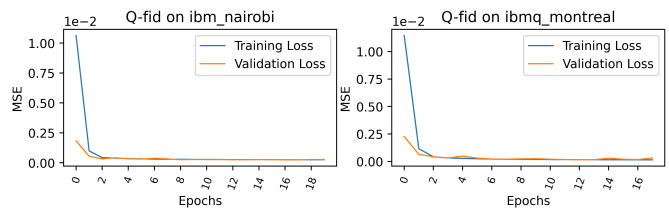


FIG. 10. Training loss and validation loss for the two datasets. Training terminated on epoch 20 for *ibm_nairobi*, and on epoch 18 for *ibmq_montreal*.

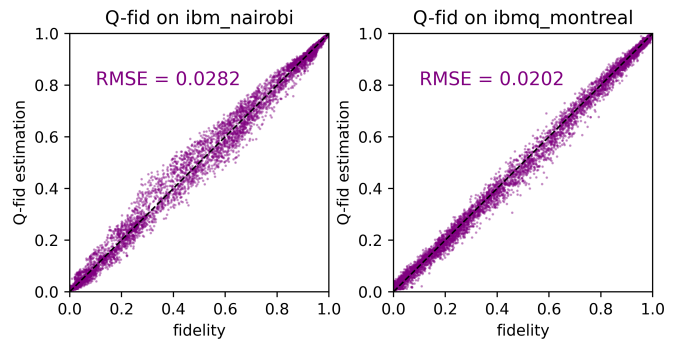


FIG. 11. Scatter plot of real fidelity vs. predicted fidelity of Q-fid running on the test set. The test set for *ibm_nairobi* contains 8,265 data points, and the test set for *ibmq_montreal* contains 9,140 data points

B. Model and Training

We build two Q-fid models to test the two processors, the architecture of Q-fid for *ibm_nairobi* is shown in figure 9. Each qubit has its own input layer and they all have a length of 500, equal to the maximum QC depth of the dataset. The embedding layer transforms every gate label into a 64-dimensional dense vector and they are all concatenated together to form one input timestep. The LSTM layer uses 256 memory units, followed by multiple fully-connected layers with shrinking hidden units to filter the features and produce the final prediction output. We use ReLU activation for filtering and Sigmoid activation for the final regression output. The model for *ibm_nairobi* contains 743,784 trainable parameters with 7 input layers, and the model for *ibmq_montreal* contains 7,403,004 trainable parameters with 27 input layers. The model for *ibmq_montreal* has mostly the same architecture, only changing the number of input layers and adding the number of hidden units.

The models are trained with a batch size of 32 plus Adam optimizer for 20 epochs using MSE loss, the training automatically terminates if the loss does not improve for 5 continuous epochs. The training, validation, and test split ratio is 7:2:1, we evaluate loss on the validation set and picked the best-performing model on the test set. The training curve for the two models is shown in figure 10, and figure 11 shows the scatter plot of real fidelity vs. predicted fidelity of Q-fid running on the test set.

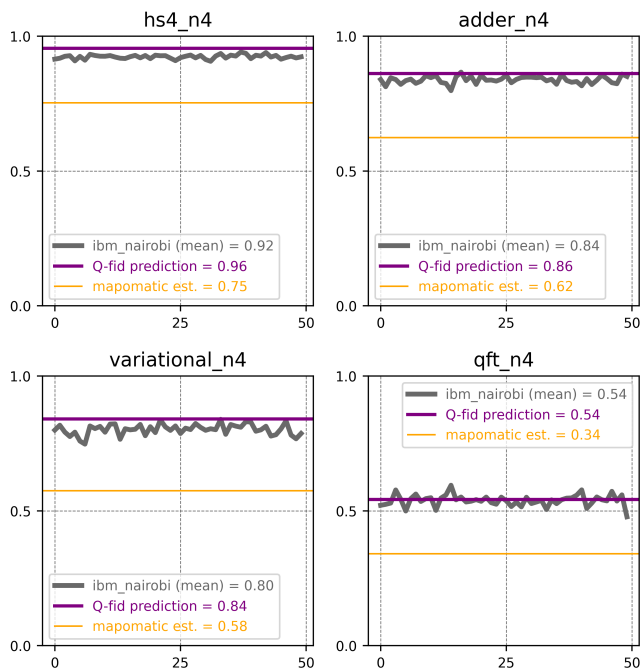


FIG. 12. Q-fid’s fidelity prediction (purple) compared with `mapomatic` (orange) on *ibm_nairobi*. Due to the probabilistic nature of quantum state measurements, the fidelity for the same circuit varies every time when executed even with the same device noise model (gray). So each quantum circuit is executed with 1,024 shots to obtain its output distribution, then repeated 50 times (x-axis) to calculate its mean fidelity. Q-fid accurately predicts the mean fidelity of each circuit.

V. RESULTS AND DISCUSSION

A. Fidelity Prediction

Based on the number of qubits, connection complexity, and algorithm practicality, we picked 25 quantum circuits from the QASMBench [16] NISQ benchmark suite to demonstrate the performance of Q-fid. Figure 12 shows four representative samples from the full result: Hidden Subgroup problem (`hs4_n4`) [31], Quantum Ripple Carry Adder (`adder_n4`) [31], Variational Ansatz (`variational_n4`) [32], and Quantum Fourier Transform (`qft_n4`) [33].

Each circuit is simulated 50 times with 1,024 shots on the Qiskit Aer simulator [34] with a noise model that mimics *ibm_nairobi*. The RMSE of Q-fid’s prediction ranges from 0.003 to 0.182 with an average of 0.0515. On the other hand, `mapomatic`’s fidelity estimation has an average RMSE of 0.142, with a minimum RMSE equal to 0.0424 and a maximum RMSE of 0.284. On the Quantum Walks algorithm (`quantumwalks_n2`) [35], Q-fid’s prediction is 24.7× more accurate than `mapomatic`.

All of the circuits in this experiment are not optimized for physical qubit layout, so the logical qubits are placed on *ibm_nairobi* in numerical order from physical qubit 0 to physical qubit 6 and stay on the same layout for all

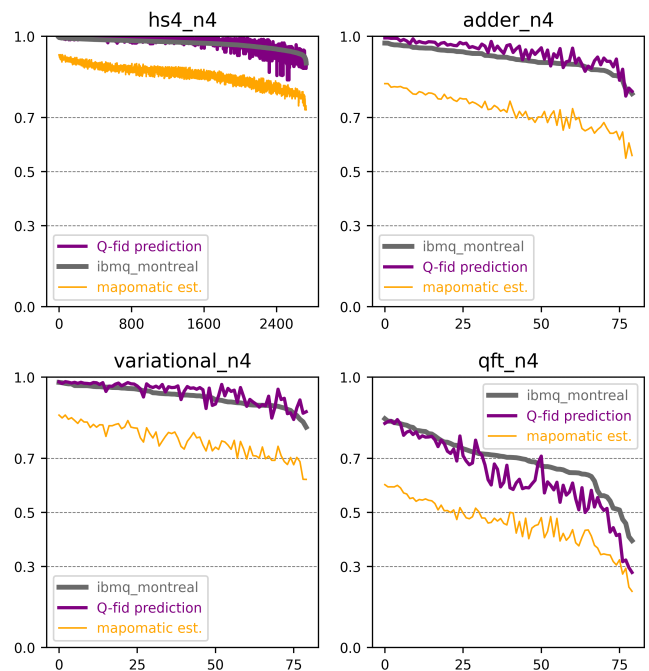


FIG. 13. Q-fid’s fidelity prediction (purple) for different circuit layouts on *ibmq_montreal*. The x-axis is the index of layouts for the quantum circuit, the y-axis shows different d - R^2 fidelity score regions listed in table I. The order of the data is sorted from the highest fidelity layout to the lowest fidelity layout according to the fidelity reported by *ibmq_montreal* (gray). Q-fid accurately tracks the fidelity variance of every layout for each circuit.

50 trials. Because most of the test circuits are using the same physical qubits, the variables in this experiment are the different quantum gates used in different algorithms. The results prove that Q-fid has learned the noise properties of different quantum gates on the same physical qubit from the dataset. In contrast, the error rate based `mapomatic` tends to give an underestimation, especially for high-fidelity circuits.

The full experiment result and data are available in Appendix A: figure 15, and table II.

B. Transpilation Optimizations

Figure 13 shows the same four sample circuits mentioned in section V A running on *ibmq_montreal*. In this experiment, the transpiler optimization is on and the physical qubit layouts are no longer fixed. Since *ibmq_montreal* is a 27-qubit processor, a circuit only using 4 physical qubits can have many available layout options depending on the number of CNOT gates it contains. For example, the `hs4_n4` circuit has a depth of 34 and 13 CNOT gates, and it has a total of 2,728 different layout executions shown in the x-axis, ranked from the highest fidelity layout to the lowest fidelity layout.

Q-fid accurately tracks the fidelity of different layouts

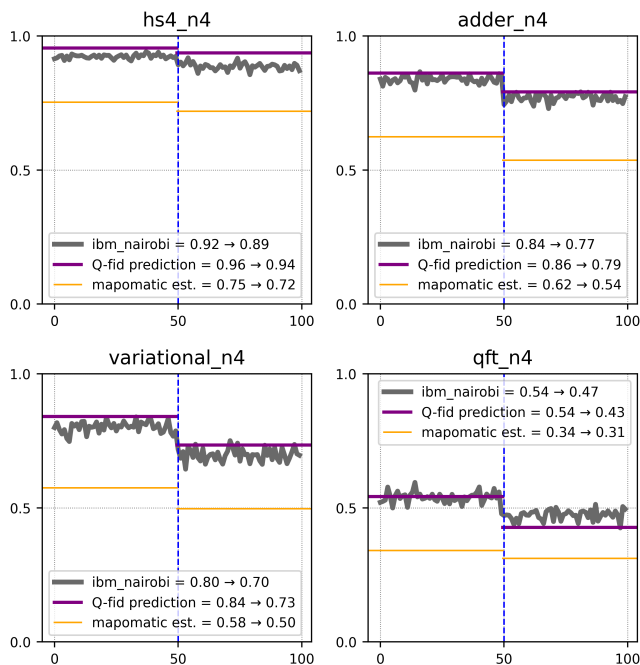


FIG. 14. Q-fid’s fidelity prediction (purple) compared with `mapomatic` (orange) on `ibm_nairobi`. The first 50 trials (left to the blue line) are performed on Nov. 15, 2022, which is the same data as in figure 12. The next 50 trials (right to the blue line) are performed on Nov. 18, 2022, which shows that `ibm_nairobi`’s performance is slightly worse due to different noise patterns. Q-fid adapts to this new noise pattern and it only takes 100 new RB samples to retrain.

for all 25 test circuits, with the number of CNOT gates in the circuits ranging from 1 to 1,419. Considering the predicted fidelities for all the layouts, Q-fid achieves an average RMSE of 0.0459, which is $5.95\times$ (up to $14.9\times$) better than `mapomatic`. When looking at only the top 10% of layouts, Q-fid achieves an average RMSE of 0.0252, which is $12.3\times$ (up to $32.8\times$) better than `mapomatic`.

An important difference should be addressed for this experiment compared with the previous experiment in section V A: In the previous experiment, the circuits are executed on fixed physical layouts, so the objective is to test if Q-fid can learn the effects of **different quantum gates** when they are applied to the **same physical qubits**. However, in this experiment, the same circuits are placed and executed with different layouts, so the new objective here is to test if Q-fid can learn the effects when the **same quantum gates** are placed on **different physical qubits**.

The full experiment result and data are available in Appendix A: figure 16, and table III.

C. Noise-adaptive Training

Since the noise characteristic of a quantum processor is constantly changing, it is important to make sure that Q-

fid can adapt to this change over time. Figure 14 shows how Q-fid can still give an accurate fidelity prediction even after the device noise model has changed. In figure 14, the same experiment in section V A is performed again, but the noise model of `ibm_nairobi` is changed to Nov. 18, 2022, three days later than the first experiment. The new noise model has a slightly worse fidelity performance than the previous one, which is shown to the right of the blue vertical line.

The RMSE of Q-fid’s new prediction ranges from 0.002 to 0.223 with an average of 0.0653. On the other hand, `mapomatic`’s new fidelity estimation has an average RMSE of 0.148, with a minimum RMSE equal to 0.0384 and a maximum RMSE of 0.287. For the new noise model, Q-fid’s prediction is $5.31\times$ more accurate than `mapomatic` on average, with the most accurate one being $42.0\times$ better.

More importantly, for Q-fid to adapt to the new noise model, the LSTM needs to be trained again with an updated dataset. In this section, the new Q-fid predictions are made after only retraining the LSTM with 100 new RB samples. Thanks to LSTM’s long-term memory capability, learning the new noise parameters on top of the previously trained model is very efficient. For `mapomatic` to update its estimation, it must use the new gate error rates calculated by performing regression analysis on the RB experiment results. In contrast, Q-fid uses the output of RB circuits directly to train its LSTM, without the need to perform any additional regression analysis or calibration measurements.

VI. CONCLUSION

In this work, we present the Q-fid system to accurately predict the fidelity of a quantum circuit running on a real NISQ processor. We show that the performance of NISQ processors is easily affected by external noise, so with Q-fid’s fidelity prediction we can help save quantum computing resources by optimizing circuit layout and reducing execution shots, all before implementing the quantum circuit on real hardware. Q-fid uses LSTM to learn the noise properties of the qubit and the relationship between quantum gates, without the need for any input of hardware calibration data and gate error rates. A novel method to represent quantum circuits using text labels was presented, and the full training workflow was introduced. We proposed a new metric called $d-R^2$ to intuitively quantify the fidelity of a noisy quantum circuit, and showed how to generate a training circuit dataset using this metric. We compared Q-fid’s performance with the `mapomatic` tool, and the results prove that Q-fid can effectively learn the characteristics of different qubits, gates, and the structure of quantum circuits.

ACKNOWLEDGMENTS

This work was supported by JST COI-NEXT Grant Number JPMJPF2221 and JST SPRING Grant Number

JPMJSP2123.

We acknowledge the use of IBM Quantum services for this work. The views expressed are those of the authors, and do not reflect the official policy or position of IBM or the IBM Quantum team.

-
- [1] D. R. Simon, *SIAM Journal on Computing* **26**, 1474 (1997), <https://doi.org/10.1137/S0097539796298637>.
- [2] F. Arute, K. Arya, R. Babbush, D. Bacon, J. C. Bardin, R. Barends, R. Biswas, S. Boixo, F. G. S. L. Brandao, D. A. Buell, B. Burkett, Y. Chen, Z. Chen, B. Chiaro, R. Collins, W. Courtney, A. Dunsworth, E. Farhi, B. Foxen, A. Fowler, C. Gidney, M. Giustina, R. Graff, K. Guerin, S. Habegger, M. P. Harrigan, M. J. Hartmann, A. Ho, M. Hoffmann, T. Huang, T. S. Humble, S. V. Isakov, E. Jeffrey, Z. Jiang, D. Kafri, K. Kechedzhi, J. Kelly, P. V. Klimov, S. Knysh, A. Korotkov, F. Kostritsa, D. Landhuis, M. Lindmark, E. Lucero, D. Lyakh, S. Mandrà, J. R. McClean, M. McEwen, A. Megrant, X. Mi, K. Michielsen, M. Mohseni, J. Mutus, O. Naaman, M. Neeley, C. Neill, M. Y. Niu, E. Ostby, A. Petukhov, J. C. Platt, C. Quintana, E. G. Rieffel, P. Roushan, N. C. Rubin, D. Sank, K. J. Satzinger, V. Smelyanskiy, K. J. Sung, M. D. Trevithick, A. Vainsencher, B. Villalonga, T. White, Z. J. Yao, P. Yeh, A. Zalcman, H. Neven, and J. M. Martinis, *Nature* **574**, 505 (2019).
- [3] C. Wang, X. Li, H. Xu, Z. Li, J. Wang, Z. Yang, Z. Mi, X. Liang, T. Su, C. Yang, G. Wang, W. Wang, Y. Li, M. Chen, C. Li, K. Linghu, J. Han, Y. Zhang, Y. Feng, Y. Song, T. Ma, J. Zhang, R. Wang, P. Zhao, W. Liu, G. Xue, Y. Jin, and H. Yu, *Transmon qubit with relaxation time exceeding 0.5 milliseconds* (2021).
- [4] A. Ortu, A. Holzäpfel, J. Etsesse, and M. Afzelius, *npj Quantum Information* **8**, 10.1038/s41534-022-00541-3 (2022).
- [5] J. Preskill, *Quantum* **2**, 79 (2018).
- [6] Z. Cai, R. Babbush, S. C. Benjamin, S. Endo, W. J. Huggins, Y. Li, J. R. McClean, and T. E. O’Brien, *Quantum error mitigation* (2022).
- [7] K. Temme, S. Bravyi, and J. M. Gambetta, *Phys. Rev. Lett.* **119**, 180509 (2017).
- [8] H.-L. Huang, X.-Y. Xu, C. Guo, G. Tian, S.-J. Wei, X. Sun, W.-S. Bao, and G.-L. Long, *Near-term quantum computing techniques: Variational quantum algorithms, error mitigation, circuit compilation, benchmarking and classical simulation* (2022).
- [9] Y. Ueno, M. Kondo, M. Tanaka, Y. Suzuki, and Y. Tabuchi, in *2021 58th ACM/IEEE Design Automation Conference (DAC)* (2021) pp. 451–456.
- [10] Y. Ueno, M. Kondo, M. Tanaka, Y. Suzuki, and Y. Tabuchi, in *2022 IEEE International Symposium on High-Performance Computer Architecture (HPCA)* (2022) pp. 274–287.
- [11] M. Y. Siraichi, V. F. dos Santos, C. Collange, and F. M. Q. Pereira, in *Proceedings of the 2018 International Symposium on Code Generation and Optimization* (ACM, 2018).
- [12] S. S. Tannu and M. K. Qureshi, in *Proceedings of the Twenty-Fourth International Conference on Architectural Support for Programming Languages and Operating Systems* (ACM, 2019).
- [13] P. D. Nation and M. Treinish, *Suppressing quantum circuit errors due to system variability* (2022).
- [14] E. Magesan, J. M. Gambetta, and J. Emerson, *Physical Review Letters* **106**, 10.1103/physrevlett.106.180504 (2011).
- [15] T. Proctor, K. Rudinger, K. Young, E. Nielsen, and R. Blume-Kohout, *Nature Physics* **18**, 75 (2021).
- [16] A. Li, S. Stein, S. Krishnamoorthy, and J. Ang, *Qasm-bench: A low-level qasm benchmark suite for nisq evaluation and simulation* (2020).
- [17] IBM, *IBM Quantum* (2021).
- [18] E. Bernstein and U. Vazirani, *SIAM Journal on Computing* **26**, 1411 (1997), <https://doi.org/10.1137/S0097539796300921>.
- [19] M. Dwarampudi and N. V. S. Reddy, *Effects of padding on lstms and cnns* (2019).
- [20] E. Magesan, J. M. Gambetta, and J. Emerson, *Physical Review A* **85**, 10.1103/physreva.85.042311 (2012).
- [21] S. Bravyi and D. Maslov, *IEEE Transactions on Information Theory* **67**, 4546 (2021).
- [22] D. Gottesman, in *Group theoretical methods in physics* (1998).
- [23] D. Chicco, M. J. Warrens, and G. Jurman, *PeerJ Computer Science* **7**, e623 (2021).
- [24] J. Liu and H. Zhou, in *2020 IEEE International Symposium on Workload Characterization (IISWC)* (2020) pp. 94–105.
- [25] D. Oliveira, E. Giusto, B. Baheri, Q. Guan, B. Montrucchio, and P. Rech, *A systematic methodology to compute the quantum vulnerability factors for quantum circuits* (2021).
- [26] T. Patel, D. Silver, and D. Tiwari, *Charter: Identifying the most-critical gate operations in quantum circuits via amplified gate reversibility* (2022).
- [27] E. Farhi, J. Goldstone, and S. Gutmann, *A quantum approximate optimization algorithm* (2014).
- [28] A. Peruzzo, J. McClean, P. Shadbolt, M.-H. Yung, X.-Q. Zhou, P. J. Love, A. Aspuru-Guzik, and J. L. O’Brien, *Nature Communications* **5**, 10.1038/ncomms5213 (2014).
- [29] A. Deshpande, P. Niroula, O. Shtanko, A. V. Gorshkov, B. Fefferman, and M. J. Gullans, *PRX Quantum* **3**, 040329 (2022).
- [30] K. Tamura and Y. Shikano, in *International Symposium on Mathematics, Quantum Theory, and Cryptography* (Springer Singapore, 2020) pp. 17–37.
- [31] A. JavadiAbhari, S. Patil, D. Kudrow, J. Heckey, A. Lvov, F. T. Chong, and M. Martonosi, in *Proceedings of the 11th ACM Conference on Computing Frontiers* (ACM, 2014).
- [32] J. R. McClean, N. C. Rubin, K. J. Sung, I. D. Kivlichan, X. Bonet-Monroig, Y. Cao, C. Dai, E. S. Fried, C. Gidney, B. Gimby, P. Gokhale, T. Häner,

- T. Hardikar, V. Havlíček, O. Higgott, C. Huang, J. Izaac, Z. Jiang, X. Liu, S. McArdle, M. Neeley, T. O'Brien, B. O'Gorman, I. Ozfidan, M. D. Radin, J. Romero, N. P. D. Sawaya, B. Senjean, K. Setia, S. Sim, D. S. Steiger, M. Steudtner, Q. Sun, W. Sun, D. Wang, F. Zhang, and R. Babbush, *Quantum Science and Technology* **5**, 034014 (2020).
- [33] A. Cross, A. Javadi-Abhari, T. Alexander, N. D. Beaudrap, L. S. Bishop, S. Heidel, C. A. Ryan, P. Sivarajah, J. Smolin, J. M. Gambetta, and B. R. Johnson, *ACM Transactions on Quantum Computing* **3**, 1 (2022).
- [34] M. Treinish, J. Gambetta, Soolu Thomas, P. Nation, Qiskit-Bot, P. Kassebaum, D. M. Rodríguez, S. De La Puente González, J. Lishman, Shaohan Hu, L. Bello, J. Garrison, K. Krsulich, Junye Huang, J. Yu, M. Marques, J. Gacon, D. McKay, E. Arellano, J. Gomez, L. Capelluto, Travis-S-IBM, A. Mitchell, A. Panigrahi, Lerongil, Rafey Iqbal Rahman, S. Wood, Toshinari Itoko, A. Pozas-Kerstjens, and C. J. Wood, *Qiskit/qiskit: Qiskit 0.42.0* (2023).
- [35] <https://github.com/raffmiceli>, Qiskit code to simulate quantum walks on graphs with up to 4 nodes, https://github.com/raffmiceli/Quantum_Walks (2020), [Accessed 16-Mar-2023].

Appendix A: Experiment Results

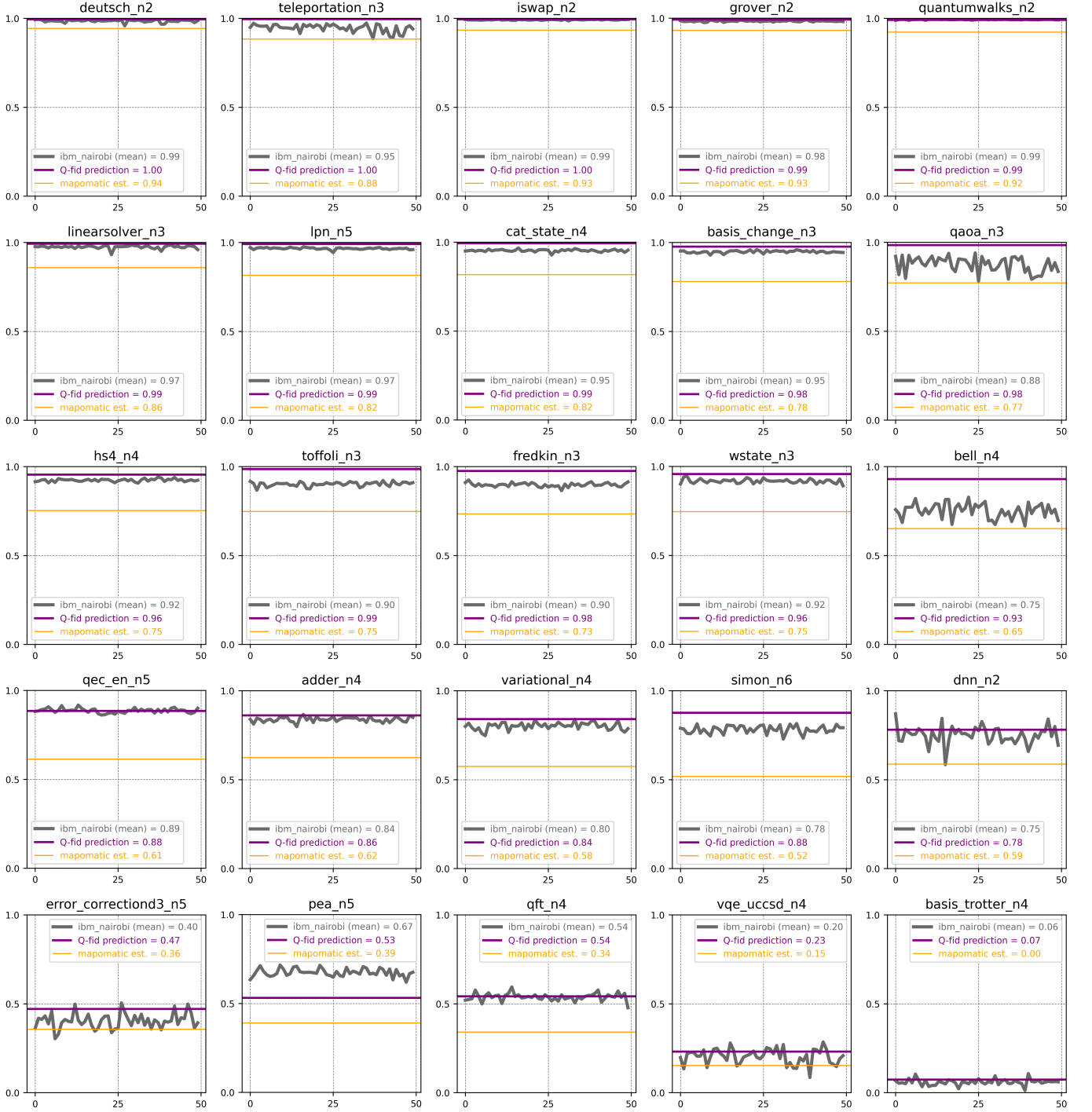


FIG. 15. Q-fid's fidelity prediction (purple) on *ibm_nairobi* compared with *mapomatic* (orange). The circuits are ranked from the lowest CNOT count (*deutsch_2*, top-left) to the highest CNOT count (*basis_trotter_n4*, bottom-right). Full data is available in table II.

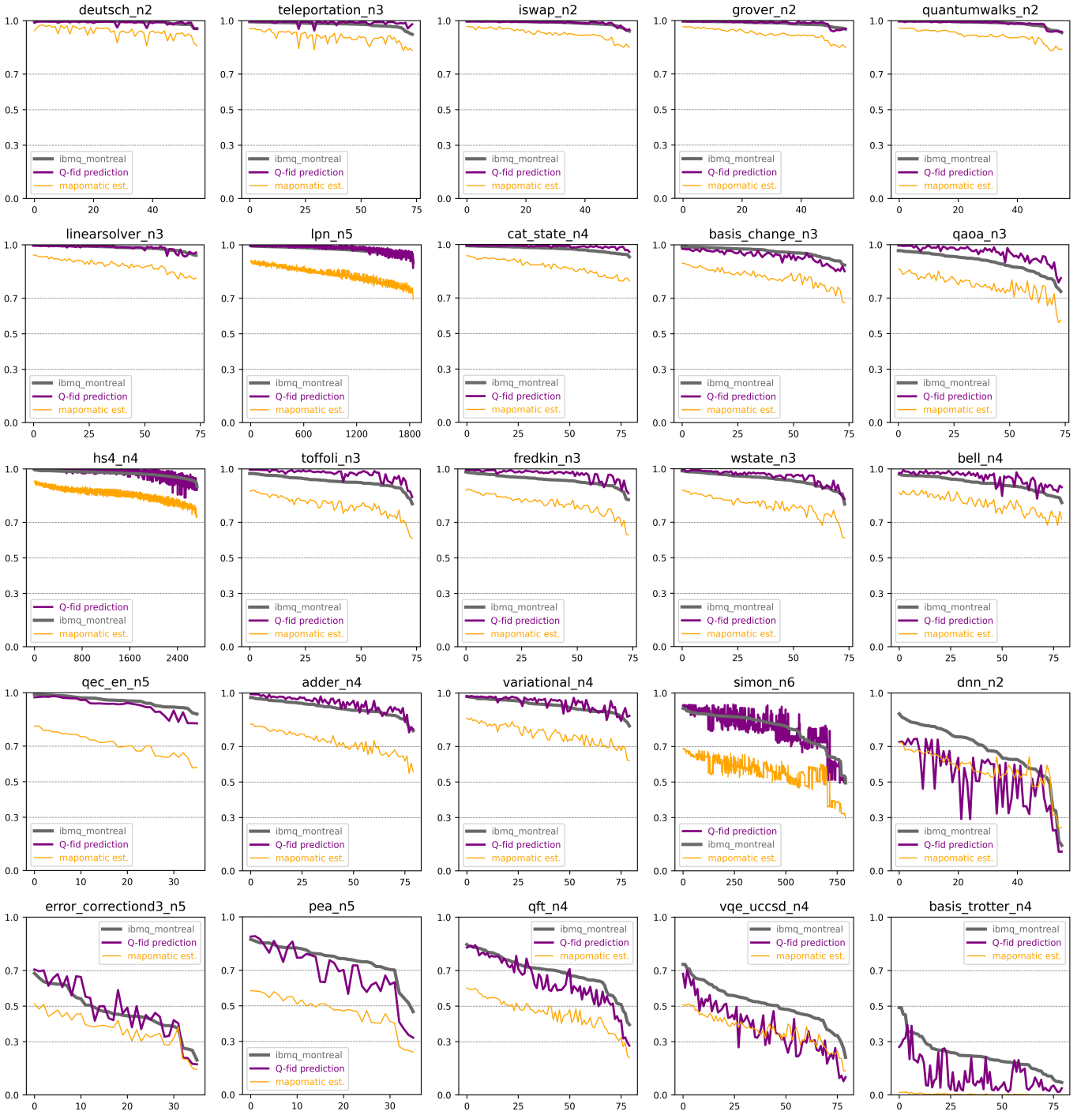


FIG. 16. Q-fid’s fidelity prediction for different circuit layouts on *ibmq_montreal*. The x-axis is the index of layouts for the quantum circuit, the y-axis shows different $d-R^2$ score regions listed in table I. The circuits are ranked from the lowest CNOT count (*deutsch_2*, top-left) to the highest CNOT count (*basis_trotter_n4*, bottom-right). Full data is available in table III.

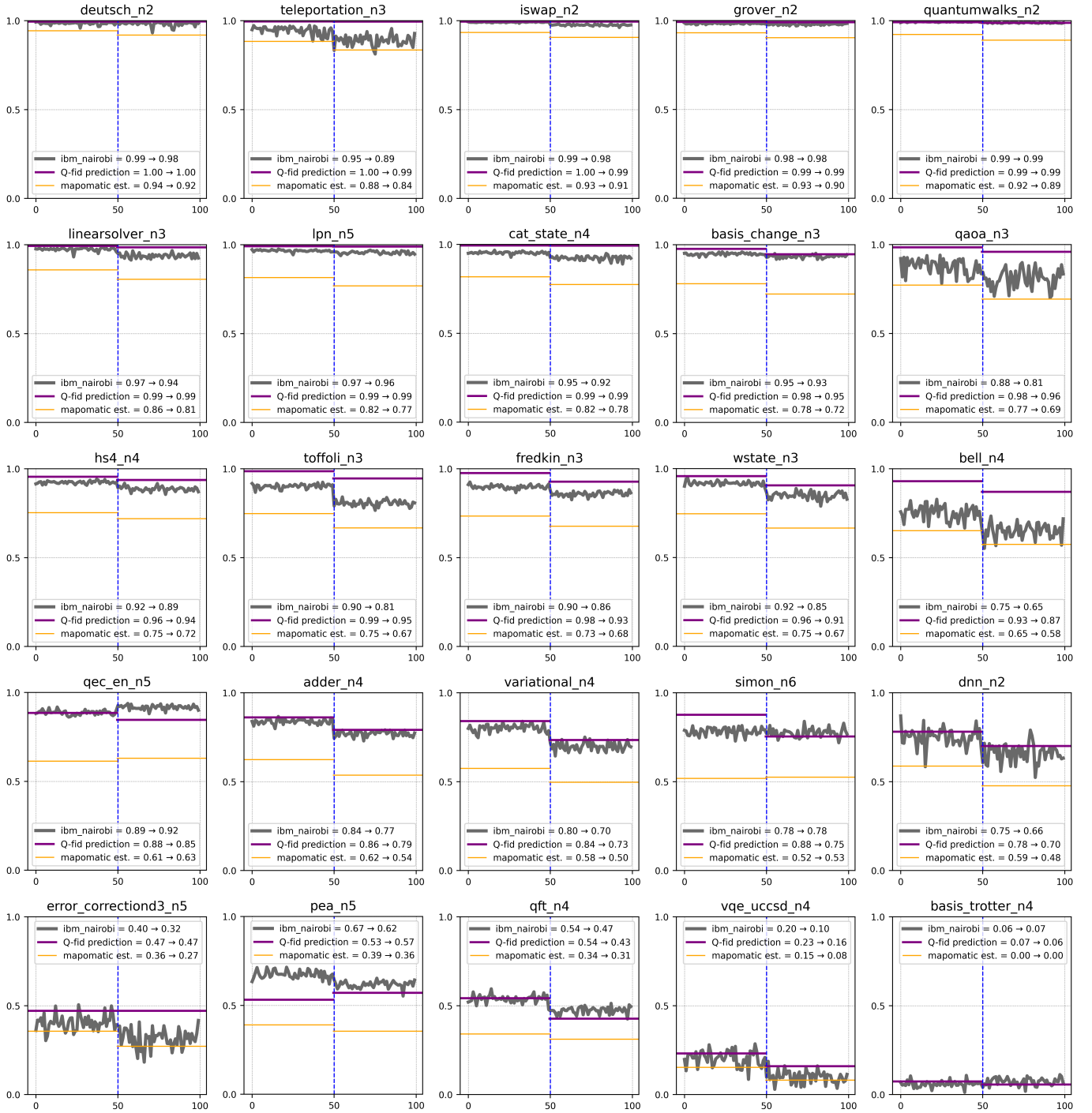


FIG. 17. Q-fid's fidelity prediction (purple) compared with mapomatic (orange) on *ibm_nairobi*. The first 50 trials (left to the blue line) are performed on Nov. 15, 2022, which is the same data as in figure 15. The next 50 trials (right to the blue line) are performed on Nov. 18, 2022, which shows that *ibm_nairobi*'s performance is slightly worse due to different noise patterns. Full data is available in table II.

	Depth	#CNOT	<i>ibm_nairobi</i> mean fidelity (11/15, 2022)	<i>mapomatic</i> prediction (11/15)	<i>mapomatic</i> RMSE (11/15)	Q-fid prediction (11/15)	Q-fid RMSE (11/15)	<i>ibm_nairobi</i> mean fidelity (11/18, 2022)	<i>mapomatic</i> prediction (11/18)	<i>mapomatic</i> RMSE (11/18)	Q-fid prediction (11/18)	Q-fid RMSE (11/18)
deutsch_n2	9	1	0.99	0.9439	4.24E-02	0.9951	1.17E-02	0.98	0.9195	6.42E-02	0.9961	1.79E-02
teleportation_n3	13	2	0.95	0.8844	6.52E-02	0.9957	5.46E-02	0.89	0.8359	6.01E-02	0.9950	1.10E-01
iswap_n2	14	2	0.99	0.9347	5.73E-02	0.9953	3.79E-03	0.98	0.9067	6.93E-02	0.9950	1.94E-02
grover_n2	26	2	0.98	0.9321	5.16E-02	0.9923	9.28E-03	0.98	0.9040	7.48E-02	0.9905	1.26E-02
quantumwalks_n2	24	3	0.99	0.9229	7.07E-02	0.9913	2.86E-03	0.99	0.8912	9.76E-02	0.9884	2.33E-03
linearsolver_n3	29	4	0.97	0.8591	1.16E-01	0.9934	2.05E-02	0.94	0.8063	1.32E-01	0.9854	4.90E-02
lpn_n5	12	5	0.97	0.8156	1.51E-01	0.9919	2.59E-02	0.96	0.7696	1.86E-01	0.9897	3.47E-02
cat_state_n4	10	6	0.95	0.8182	1.35E-01	0.9944	4.16E-02	0.92	0.7750	1.49E-01	0.9933	7.06E-02
basis_change_n3	114	10	0.95	0.7811	1.67E-01	0.9769	2.94E-02	0.93	0.7231	2.12E-01	0.9463	1.42E-02
qaoa_n3	24	12	0.88	0.7729	1.12E-01	0.9846	1.17E-01	0.81	0.6942	1.26E-01	0.9599	1.59E-01
hs4_n4	34	13	0.92	0.7539	1.70E-01	0.9552	3.20E-02	0.89	0.7201	1.67E-01	0.9368	5.12E-02
toffoli_n3	23	15	0.90	0.7483	1.54E-01	0.9863	8.49E-02	0.81	0.6681	1.39E-01	0.9460	1.41E-01
fredkin_n3	25	17	0.90	0.7344	1.64E-01	0.9764	7.89E-02	0.86	0.6773	1.83E-01	0.9280	6.98E-02
wstate_n3	37	18	0.92	0.7464	1.72E-01	0.9575	4.12E-02	0.85	0.6659	1.84E-01	0.9060	6.06E-02
bell_n4	62	25	0.75	0.6524	1.08E-01	0.9301	1.82E-01	0.65	0.5750	8.55E-02	0.8707	2.23E-01
qec_en_n5	45	31	0.89	0.6143	2.73E-01	0.8848	1.26E-02	0.92	0.6307	2.87E-01	0.8459	7.22E-02
adder_n4	48	40	0.84	0.6246	2.14E-01	0.8616	2.67E-02	0.77	0.5373	2.34E-01	0.7916	2.62E-02
variational_n4	70	40	0.80	0.5756	2.27E-01	0.841	4.38E-02	0.70	0.4970	2.03E-01	0.7343	4.28E-02
simon_n6	57	41	0.78	0.5188	2.65E-01	0.8762	9.60E-02	0.78	0.5263	2.50E-01	0.7543	3.15E-02
dnn_n2	499	42	0.75	0.5883	1.70E-01	0.7814	5.77E-02	0.66	0.4773	1.90E-01	0.7011	6.53E-02
error_correctiond3_n5	163	79	0.40	0.3572	6.36E-02	0.4715	7.94E-02	0.32	0.2726	6.92E-02	0.4710	1.63E-01
pea_n5	121	84	0.67	0.3910	2.84E-01	0.5322	1.44E-01	0.62	0.3556	2.63E-01	0.5713	5.01E-02
qft_n4	132	87	0.54	0.3414	1.99E-01	0.5424	2.10E-02	0.47	0.3119	1.63E-01	0.4273	5.00E-02
vqe_uccsd_n4	351	166	0.20	0.1532	6.66E-02	0.2312	4.98E-02	0.10	0.0814	3.84E-02	0.1593	6.90E-02
basis_trotter_n4	2593	1419	0.06	0.0000	6.22E-02	0.0739	2.19E-02	0.07	0.0000	7.59E-02	0.0566	2.62E-02

TABLE II. Fidelity prediction data corresponding to figure 15 and figure 17.

	<i>ibmq_montreal</i> fidelity range	#Layouts (all)	<i>mapomatic</i> RMSE (all)	Q-fid RMSE (all)	#Layouts (top 10%)	<i>mapomatic</i> RMSE (top 10%)	Q-fid RMSE (top 10%)
deutsch_n2	1.00-0.96	56	5.965E-02	8.395E-03	6	3.409E-02	5.438E-03
teleportation_n3	0.99-0.92	74	7.552E-02	1.660E-02	7	4.285E-02	2.216E-03
iswap_n2	1.00-0.94	56	6.327E-02	4.743E-03	6	3.715E-02	3.496E-03
grover_n2	1.00-0.95	56	6.307E-02	7.142E-03	6	3.381E-02	1.458E-03
quantumwalks_n2	1.00-0.93	56	7.280E-02	4.874E-03	6	4.109E-02	3.736E-03
linearsolver_n3	1.00-0.94	74	1.009E-01	8.393E-03	7	6.113E-02	3.097E-03
lpn_n5	1.00-0.90	1840	1.400E-01	1.131E-02	184	9.545E-02	2.911E-03
cat_state_n4	0.99-0.93	80	1.034E-01	1.724E-02	8	6.539E-02	2.597E-03
basis_change_n3	0.99-0.89	74	1.438E-01	2.727E-02	7	1.023E-01	1.511E-02
qaoa_n3	0.97-0.74	74	1.322E-01	5.724E-02	7	1.148E-01	3.079E-02
hs4_n4	1.00-0.90	2728	1.191E-01	1.388E-02	273	8.007E-02	2.522E-03
toffoli_n3	0.97-0.80	74	1.367E-01	4.377E-02	7	1.013E-01	2.356E-02
fredkin_n3	0.98-0.83	74	1.356E-01	3.650E-02	7	1.012E-01	1.633E-02
wstate_n3	0.99-0.80	74	1.486E-01	2.166E-02	7	1.154E-01	7.731E-03
bell_n4	0.97-0.81	80	1.154E-01	3.922E-02	8	1.002E-01	1.889E-02
qec_en_n5	0.99-0.88	36	2.453E-01	3.329E-02	4	1.896E-01	1.345E-02
adder_n4	0.98-0.79	80	1.934E-01	2.981E-02	8	1.542E-01	2.102E-02
variational_n4	0.98-0.82	80	1.633E-01	2.617E-02	8	1.273E-01	7.697E-03
simon_n6	0.91-0.49	792	2.530E-01	5.100E-02	79	2.363E-01	2.280E-02
dnn_n2	0.88-0.14	56	1.285E-01	1.873E-01	6	1.622E-01	1.292E-01
error_correctiond3_n5	0.68-0.20	36	1.129E-01	5.624E-02	4	1.675E-01	3.887E-02
pea_n5	0.87-0.47	36	2.900E-01	9.605E-02	4	2.817E-01	2.029E-02
qft_n4	0.85-0.40	80	2.361E-01	7.141E-02	8	2.429E-01	1.835E-02
vqe_uccsd_n4	0.73-0.21	80	1.536E-01	1.467E-01	8	1.965E-01	7.047E-02
basis_trotter_n4	0.49-0.07	80	2.345E-01	1.319E-01	8	4.042E-01	1.486E-01

TABLE III. Transpilation optimization data corresponding to figure 16.